

## RESEARCH ARTICLE

# HRMAN 2.0: Next-generation artificial intelligence-driven analysis for broad host–pathogen interactions

Daniel Fisch<sup>1,2</sup>  | Robert Evans<sup>1,2</sup> | Barbara Clough<sup>1</sup> | Sophie K. Byrne<sup>1</sup> | Will M. Channell<sup>1</sup> | Jacob Dockterman<sup>3</sup> | Eva-Maria Frickel<sup>1</sup> 

<sup>1</sup>Institute of Microbiology and Infection, School of Biosciences, University of Birmingham, Edgbaston, UK

<sup>2</sup>Host-Toxoplasma Interaction Laboratory, The Francis Crick Institute, London, UK

<sup>3</sup>Department of Immunology, Duke University Medical Center, Durham, North Carolina

## Correspondence

Eva-Maria Frickel, Institute of Microbiology and Infection, School of Biosciences, University of Birmingham, Edgbaston B15 2TT, UK.

Email: e.frickel@bham.ac.uk

Daniel Fisch, Institute of Microbiology and Infection, School of Biosciences, University of Birmingham, Edgbaston B15 2TT, UK.  
Email: daniel.fisch@crick.ac.uk

## Funding information

Boehringer Ingelheim Fonds; Cancer Research UK, Grant/Award Number: FC00107; Medical Research Council, Grant/Award Number: FC00107; Wellcome Trust, Grant/Award Numbers: 217202/Z/19/Z, FC00107

## Abstract

To study the dynamics of infection processes, it is common to manually enumerate imaging-based infection assays. However, manual counting of events from imaging data is biased, error-prone and a laborious task. We recently presented HRMAN (Host Response to Microbe Analysis), an automated image analysis program using state-of-the-art machine learning and artificial intelligence algorithms to analyse pathogen growth and host defence behaviour. With HRMAN, we can quantify intracellular infection by pathogens such as *Toxoplasma gondii* and *Salmonella* in a variety of cell types in an unbiased and highly reproducible manner, measuring multiple parameters including pathogen growth, pathogen killing and activation of host cell defences. Since HRMAN is based on the KNIME Analytics platform, it can easily be adapted to work with other pathogens and produce more readouts from quantitative imaging data. Here we showcase improvements to HRMAN resulting in the release of HRMAN 2.0 and new applications of HRMAN 2.0 for the analysis of host–pathogen interactions using the established pathogen *T. gondii* and further extend it for use with the bacterial pathogen *Chlamydia trachomatis* and the fungal pathogen *Cryptococcus neoformans*.

## KEYWORDS

artificial intelligence, host–pathogen interaction, image analysis

## 1 | INTRODUCTION

Pathogen infection of cells can be analysed by fluorescence microscopy and relies on accurate quantification of observed phenotypes to reveal magnitudes of host and pathogen parameters and the kinetics of their interaction. Manual scoring of infection processes from microscopy images is laborious, biased and prone to errors. Often, it restricts the number of samples and replicates that are included in an experiment (Meijering, Carpenter, Peng, Hamprecht, & Olivo-Marin, 2016).

High-throughput image acquisition with automated high-content imaging platforms opens the possibility of studying host–pathogen interactions on a large scale (Pegoraro & Misteli, 2017), for instance in combination with genome-wide depletion screens (Brodin & Christophe, 2011; Usaj et al., 2016). However, our ability to produce huge imaging datasets is curtailed by our ability to analyse them efficiently and accurately (Meijering et al., 2016).

Innovation in automated image analysis has relied on either open-source (Carpenter et al., 2006; Smith et al., 2018; Stöter et al., 2013) or proprietary (e.g., Perkin Elmer Harmony) software for analysis. Typically, images are analysed by classical fixed-parameter image

Daniel Fisch and Robert Evans contributed equally to this work.

This is an open access article under the terms of the Creative Commons Attribution License, which permits use, distribution and reproduction in any medium, provided the original work is properly cited.

© 2021 The Authors. *Cellular Microbiology* published by John Wiley & Sons Ltd.

segmentation algorithms (Kühbacher et al., 2015; Matula et al., 2009; Osaka et al., 2012). However, data generated by these classical approaches are usually restricted to quantifying the pathogen growth on a single-cell level. Extracting information beyond this uppermost layer of host–pathogen interactions, for example, analysing the redistribution of proteins upon infection, is difficult due to the inherent heterogeneity of imaging datasets and cellular responses. Furthermore, classic image segmentation approaches are dataset specific and require manually altering the segmentation parameters (i.e., updating the code/parameters of the program) to produce reliable data, for instance, the cell type or nature and/or intensity of stainings change between experiments.

To overcome these limitations and enable infection researchers to quantify their imaging data without the need for coding, we created HRMAN (Host Response to Microbe Analysis) (Fisch et al., 2019). HRMAN is a high-throughput, high-content, single-cell image analysis pipeline that incorporates machine learning (ML) and an ensemble of deep convolutional neural network (CNN) for infection analysis ([www.hrman.org](http://www.hrman.org)). To assure its broad usability and future software support, HRMAN is based on the data handling environment KNIME Analytics platform (Berthold et al., 2008). The analysis relies on training of ML algorithms and deep CNNs that can be tailored to individual researchers' needs and experimental questions. The trained CNNs contained within the analysis pipeline are used for image classification, phenotype quantification and for instance segmentation, a hybrid of semantic segmentation and object detection. CNNs work with the image itself and make use of complex patterns (e.g., shapes) within the dataset to learn phenotypes which they derive in a supervised fashion from expert-labelled data (Krizhevsky, Sutskever, & Hinton, 2012). Deep CNNs consist of several layers, mimicking the cortex of a brain. These can comprise convolution, normalisation, pooling and fully connected layers (Nielsen, 2015) which convolve features, normalise for local contrast enhancement (Krizhevsky et al., 2012) or down sample feature maps to increase the sensitivity of the network. Combining several of these layers all looking at the output maps of the previous layer creates a deep CNN that step-by-step reduces the complexity of the input, size of the tensor and extracts key features and patterns. In deep CNNs for classification, the final layers are usually fully connected layers, which produce the output (for an excellent overview please refer to LeCun, Bengio, & Hinton, 2015). Use of AI for image analysis allows for increased flexibility and versatility of HRMAN 2.0, without requiring the user to update the code and analysis parameters for every dataset (Godínez, Hossain, Lazic, Davies, & Zhang, 2017; Kraus et al., 2017; Kraus, Ba, & Frey, 2016).

HRMAN was designed for quantification of high-content imaging experiments and has direct compatibility with datasets from 96-well or 384-well cell culture plates. Prior to analysis, stained specimens (infected host cells) are imaged on a fluorescence microscope. Ideally, the use of automated high-throughput imaging platforms allows for rapid acquisition of images from multi-well plates, but standard fluorescence imagers with a programmable stage can also be used for image acquisition (reviewed in Fisch, Yakimovich, Clough, Mercer, & Frickel, 2020).

## TAKE AWAY

- HRMAN 2.0 allows host-pathogen interaction analysis from imaging experiments
- HRMAN 2.0 extends the analysis into the 3D-space
- HRMAN 2.0 can be adapted for analysis of any intracellular pathogen
- HRMAN 2.0 uses AI for focus detection, segmentation and phenotype quantification

Depending on the type of experiment, HRMAN allows the user to choose from a range of analysis methods (Fisch et al., 2019). Simple infection analysis only assesses host cell and pathogen numbers as well as replication of the pathogens. This fast analysis provides the same quantification as would have classically been obtained by manual counting, but in a matter of minutes, for thousands of images, rather than hours/days. Further insight into host–pathogen interactions can be gained by studying the changing spatial distribution of host and pathogen proteins, but quantifying this manually or by using classical image analysis approaches is close to impossible. HRMAN therefore relies on ML and deep CNNs to classify and quantify localization of proteins on a single-cell level. Readouts from this second stage of analysis represent one of the more advanced analysis methods offered by HRMAN (Fisch et al., 2019).

Two years ago, we presented the original HRMAN (Fisch et al., 2019). Continued development of HRMAN now allows us to release HRMAN 2.0 an even more powerful ensemble of ML and artificial intelligence algorithms for image analysis/quantification. In this work, we present the major improvements and additions to the original HRMAN and illustrate how HRMAN 2.0 can be used in new ways to dissect the interaction between host cells and intracellular pathogens. We also present methods of ongoing data collection which involve crowdsourcing classifications from non-expert volunteers. Volunteer consensus data from the Zooniverse platform (<https://www.zooniverse.org>) will be used in conjunction with pooled training data generated by experts, to create unbiased CNN training datasets for the continued development of HRMAN.

## 2 | RESULTS

### 2.1 | Improved input/output

HRMAN was originally designed to reliably and automatically quantify host–pathogen interactions on a large scale. Now, HRMAN 2.0 has a more streamlined user interface that guides the users through the setup and additionally performs quality control on input images before analysis commences (Figure 1a). The execution process (order, timings, memory management) of HRMAN 2.0 has been improved leading

(a)

**WELCOME TO HRMAN**  
Please follow the instructions below, step-by-step

1. Select file upload node and input the directory with the images that should be analysed. (When using Bulk upload for the information, also provide this file here.
2. Select the node below and execute it. Please input all necessary information in the pop-up dialogue windows
3. Select the Image Viewer Node and execute it. Once done, please inspect that all images have been loaded and organised correctly.
4. Select the Interactive Segmentation View node and execute it. Once finished, please make sure that the nuclei have been segmented correctly.
5. Select the Interactive Segmentation View node and execute it. Once finished, please make sure that the pathogens have been segmented correctly.
6. Select the Interactive Segmentation View node and execute it. Once finished, please make sure that the cells have been segmented correctly.
7. If all segmentations are satisfactory, please select the node below and execute it. All results will be written to the directory where the original image folder was located.
8. If needed, select the node below and execute it. The node will provide a quick overview of the calculated results.

File Upload, File Upload, Bulk Upload information, Load data and pre-process, Segmentation, Input Images, Interactive Segmentation View, Nuclei labels, Interactive Segmentation View, Pathogen labels, Interactive Segmentation View, Cell labels, Do calculation and write results, Data Dashboard

Once an analysis has finished reset the workflow and close KNIME. Do NOT save while the workflow has data in it! If you want to run a new analysis please re-start KNIME (otherwise the built-up of temporary files will cause the analysis to fail).

(b)

**Analysis**

Please choose the Analysis type:

- Infection analysis
- Recruitment analysis
- 3D Infection-Analysis (uses Cellpose)
- Co-Localisation
- Co-Infection
- Protein localisation (Nucleus vs. Cytosol)
- 3D Recruitment-Analysis (uses Cellpose)

OK

**Assay Layout**

Please insert your sample groups into the assay layout:

	01	02	03	04	05	06	07	08	09	10	11	12
A	0	0	0	0	0	0	0	0	0	0	0	0
B	0	1	2	3	4	5	6	7	8	9	10	0
C	0	1	2	3	4	5	6	7	8	9	10	0
D	0	1	2	3	4	5	6	7	8	9	10	0
E	0	1	2	3	4	5	6	7	8	9	10	0
F	0	1	2	3	4	5	6	7	8	9	10	0
G	0	1	2	3	4	5	6	7	8	9	10	0
H	0	0	0	0	0	0	0	0	0	0	0	0

Make sure to only add numbers

OK

(c)

	Infection analysis	Recruitment analysis	3D-infection analysis	3D-Recruitment analysis	Protein localisation
Channels	3	3/4 for dual channel recruitment	3	3/4 for dual channel recruitment	3/4 for dual channel distribution of proteins
Segmentation	User choice	User choice	3D-Cellpose	3D-Cellpose	User choice
Brightfield for cells?	Yes	Yes	Yes (not recommended)	Yes (not recommended)	Yes
Cell features	Geometry (Size, Circularity, Perimeter, Convexity, Diameter, Extend), Fluorescence (Mean, Min, Max, Geometric Mean, Sum)	Geometry (Size, Circularity, Perimeter, Convexity, Diameter, Extend), Fluorescence (Mean, Min, Max, Geometric Mean, Sum)	Geometry (Size, Circularity, Perimeter, Convexity, Diameter, Extend), Fluorescence (Mean, Min, Max, Geometric Mean, Sum)	Geometry (Size, Circularity, Perimeter, Convexity, Diameter, Extend), Fluorescence (Mean, Min, Max, Geometric Mean, Sum)	Geometry (Size, Circularity, Perimeter, Convexity, Diameter, Extend), Fluorescence (Mean, Min, Max, Geometric Mean, Sum)
Pathogen features	Geometry (Size, Circularity, Perimeter, Convexity, Diameter, Extend), Fluorescence (Mean, Min, Max, Geometric Mean, Sum)	Geometry (Size, Circularity, Perimeter, Convexity, Diameter, Extend), Fluorescence (Mean, Min, Max, Geometric Mean, Sum)	Geometry (Size, Circularity, Perimeter, Convexity, Diameter, Extend), Fluorescence (Mean, Min, Max, Geometric Mean, Sum)	Geometry (Size, Circularity, Perimeter, Convexity, Diameter, Extend), Fluorescence (Mean, Min, Max, Geometric Mean, Sum)	Geometry (Size, Circularity, Perimeter, Convexity, Diameter, Extend), Fluorescence (Mean, Min, Max, Geometric Mean, Sum)
Counting	Cell number, Vacuole number, Pathogen number	Cell number, Vacuole number, Pathogen number	Cell number, Vacuole number, Pathogen number	Cell number, Vacuole number, Pathogen number	Cell number, Vacuole number, Pathogen number
%Infected cells	+	+	+	+	+
Infection levels/distribution	+	+	+	+	+
Vacuole:Cell ratio	+	+	+	+	+
Pathogen load	+	+	+	+	+
%Replicating pathogens	+	+	+	+	+
Replication distribution	+	+	+	+	+
Vacuole position	+	+	+	+	+
Inter vacuole distance (single cell)	+	+	+	+	+
Inter cell distance	+	+	+	+	+
Fluorescence reporter cytosol	-	-	-	-	+
Fluorescence reporter nucleus	-	-	-	-	+
Ratio fluorescence nucleus/cytosol	-	-	-	-	+
Number of planes pathogen/cell was detected	-	-	+	+	-
Number of planes pathogen recruitment was analysed in	-	-	-	+	-
Recruitment numbers	-	+	-	+	-
Co-Recruitment	-	Yes, for 4 channels	-	Yes, for 4 channels	-
%Recruiting cells	-	+	-	+	-
Recruited vacuoles per cell	-	+	-	+	-
Protein recruitment levels	-	+	-	+	-
Vacuole coat distance	-	+	-	+	-
Vacuole coat thickness	-	+	-	+	-
%Replicating pathogens (recruited)	-	+	-	+	-
Replication distribution (recruited)	-	+	-	+	-
Confidence in replication prediction	+	+	+	+	+
Confidence in recruitment prediction	-	+	-	+	-
Mean Focus quality + PLLS	+	+	+	+	+
Validated pathogens	<i>Toxoplasma gondii</i> , <i>Salmonella</i> , <i>EPEC</i> , <i>Mycobacterium</i> , <i>Shigella</i> , <i>Listeria</i> , <i>Cryptococcus</i> , <i>Trypanosoma</i> , <i>Chlamydia</i> , <i>UPEC</i> , <i>Aspergillus</i>	<i>Toxoplasma gondii</i> , <i>Salmonella</i> , <i>Cryptococcus</i> , <i>Chlamydia</i>	<i>Toxoplasma gondii</i> , <i>Salmonella</i> , <i>Cryptococcus</i>	<i>Toxoplasma gondii</i> , <i>Salmonella</i>	<i>Toxoplasma gondii</i> , <i>Salmonella</i>

FIGURE 1 Legend on next page.

to overall shorter analysis times and more stability of the program. Lastly, many parameter-extraction/-adjustment processes have been automated and user input/output has been simplified and made more graphical, for example, by including a user interface for defining the assay layout (Figure 1b). Therefore, users now exclusively need to direct the program to their image input directory, select their analysis method and pathogen (Figure 1c) and the rest will be managed automatically. For an overview of all changes and improvements see Table 1.

In summary, the updated input/output system of HRMAN 2.0 makes it easier for the user to follow the analysis and assess whether the program is working accurately. The updates also improve performance and facilitate ease-of-use while maintaining accuracy and unbiased analysis capabilities. Since image analysis is computationally expensive, please refer to Table 2 for minimal and recommended system requirements to run HRMAN 2.0 with and without GPU acceleration and for an overview of expected analysis times for datasets of different sizes.

## 2.2 | New image pre-processing

Image data pre-processing is important for any kind of large-scale imaging-based experiment (Bray, Fraser, Hasaka, & Carpenter, 2012). The original HRMAN already performed single-channel illumination corrections, and this step has not been changed as it was performing well (Fisch et al., 2019). Briefly, HRMAN 2.0 performs channel-wise, retrospective illumination correction, by creating a bright image without objects using a low-pass filter with a large kernel (Gaussian) and subtracting this as background. Additionally, HRMAN 2.0 now pre-screens images for contamination/imaging artefacts and for out-of-focus images. These images need to be removed from the analysis since they can, in the worst case, affect the quality of an experiment/screen overall.

In order to do this, we implemented calculation of the percent maximum metric for each image, as suggested by Bray et al. (2012), into HRMAN 2.0 to exclude images with saturation artefacts. Furthermore, we added a two-tier focus quality detection strategy to HRMAN 2.0. In tier one, HRMAN 2.0 uses an artificial intelligence approach as has been proposed and spearheaded by Yang et al. (2018) to judge image quality. For tier one analysis, we trained a deep neural network that works on  $300 \times 300$  px tiles of the input image of the cell nuclei and bins them into classes between 0 (in-focus) and 10 (out-of-focus) (Figure 2a). Finally, for each individual image, the overall focus class is calculated as a mean of the respective image tiles (Figure 2a). We trained the neural network with more than 500,000 images that were

either in focus or artificially defocused as described by Yang et al. (2018) and furthermore injected with Poisson noise to allow for training of a more generalised model (Figure 2b). The final model obtained after training was >95% accurate in classifying previously unseen images (Figure 2b). The CNN-based quality assessment is complemented in tier 2 by calculation of the power Log-Log Slope (PLLS) which measures the slope of the power spectrum density of intensities within an image (Bray et al., 2012). Combination of two independent focus detection strategies now allows HRMAN to precisely pre-filter images prior to analysis (Bray et al., 2012; Groen, Young, & Ligthart, 1985; Sun, Duthaler, & Nelson, 2004; Yang et al., 2018). To do so, we have pre-configured HRMAN 2.0 to select images with a focus that is deemed acceptable to produce reliable results in the downstream analysis steps. However, these thresholds can be changed by the user, if a more stringent filtering is required or vice versa.

Indeed, combining the two tiers into one focus-quality assessment strategy allowed us to accurately filter images in a larger experiment that used images from 360 positions each with 16 different focus positions (Figure 2c). Since HRMAN 2.0 was also set up to perform 3D analysis, the two-tiered focus determination method allows for selection of the most in-focus planes in a series of z-stacks (Figure 2d). We illustrated this in an experiment that on purpose had a multi-well plate mounted in a high-content imager in a slight tilt. Here, HRMAN 2.0, depending on the analysis type, was able to reject individual fields, as would be the case in a 2D-experiment/analysis, or correctly pick the most in focus images in the z-stack series when run in 3D analysis mode (Figure 2e). We designed HRMAN 2.0 to automatically connect to a remote CNN model repository to obtain the trained focus-detection CNN without the user having to provide it manually. Furthermore, HRMAN 2.0 reports which fields have not passed the quality control (and have therefore been excluded) to the user and appends image quality notes into the results file for the user to inspect subsets of their dataset that have been flagged and excluded from the analysis.

## 2.3 | Improved object detection by instance segmentation using trained CNNs

The original version of HRMAN relied on classical, thresholding-based segmentation for object detection (e.g., cells, nuclei and pathogens) before performing quantification of the images and the host-pathogen interaction as well as host protein to pathogen recruitment analysis using a CNN. While this was reliable for many different imaging datasets, we added options to perform object detection using

**FIGURE 1** The HRMAN 2.0 graphical user interface and analysis capabilities. The graphical user interface of HRMAN 2.0 (a) has been streamlined to better guide the user through the analysis steps. Furthermore, entering the parameters of an analysis has been simplified by addition of interactive menus, including list selections of analysis types and the graphical representation of multi-well plates to define the assay layout (b). HRMAN 2.0 has different analysis methods, and the table in (c) provides an overview of settings, calculated readouts and pathogens for which the analysis has already been validated for

**TABLE 1** Improvements of HRMAN 2.0 as compared to the previous version

HRMAN 1.0	Upgrades for HRMAN 2.0
Manual input of image information to setup analysis parameters	Image information is detected automatically. Information that cannot be detected is entered by user via pop-up dialogue boxes. (Magnification, pixel size, number and order of channels, pathogen type, analysis type and segmentation methods)
Assay layout uploaded as a counterintuitive spreadsheet file	Clear graphical user interface that allows users to input assay layouts (96-well and 384-well plates) with better overview. Additionally, users can create customisable layouts for images from coverslips
No bulk input option for large-scale analysis	Bulk upload option from template to circumvent manual parameter input for faster, large-scale analysis
Simple inspection of segmentations as quality control	Streamlined layout of the analysis pipeline to encourage quality inspection by the user and better display of segmentations in an interactive view showing overlays of original data and detected objects
No memory management, causing instability on less powerful computer systems	Chunking of data and memory/temporary file management for increased stability of the analysis pipeline
No updates on progress of the analysis	Visual messages in the KNIME console inform users on the progress of the analysis. Acoustic signals when analysis steps are done.
Manual upload of a reference dataset for ML prediction of pathogen replication	Automatic choice of reference dataset for ML prediction of pathogen replication
Images to be named in a plate format, required pre-formatting with separate workflow	All-in-one pipeline that automatically arranges images and requires no pre-formatting of images
No support for 3D datasets	Automated z-projections if 2D analysis is to be performed, option for full 3D analysis
Manual removal of corrupted files prior to executing the analysis pipeline	Automated removal of corrupted images, replacement by empty fields of view using same data structure
Unchanged input data folder	Automated archiving of input images for long-term storage of raw data following the analysis
Manual creation of several empty output files to save data following the analysis	Automated creation of a single spreadsheet output file which contains all calculated results
Storage of only the grouped final results	Storage of all calculated results (assay layout, analysis parameters, data quality, data for each individual cell and pathogen, grouped data for each field, well/coverslip and the sample groups overall)
No information on quality of ML/AI performance	Report of confidence values for prediction of pathogen replication and for protein recruitment analysis with CNN (Allows judging of performance by the user)
No reporting of label IDs	Reporting of unique labels IDs that allows tracing each label back to the raw data
No data inspection capability within HRMAN	Interactive data dashboard for fast inspection of key data and statistics
Manual upload of trained CNN models	Automated download of latest models from central repository
No news on new updates	Automated messages inform users about availability of newer versions
Simple CUDA GPU acceleration	Enhanced GPU-acceleration for maximum performance and stability when using GPU for calculations

artificial intelligence in HRMAN 2.0, greatly increasing the program's versatility (Caicedo et al., 2019). To do so, we have implemented an adapted version of StarDist for nuclei segmentation (Schmidt, Weigert, Broaddus, & Myers, 2018) and a full version of Cellpose for (label-free) cell segmentation (Figure S1) (Stringer, Wang, Michaelos, & Pachitariu, 2021).

In brief, StarDist combines a CNN with non-maxima-suppression (NMS) to segment nuclei from fluorescence images (Schmidt et al., 2018). Unfortunately, we were not able to perform NMS within KNIME while maintaining ease of use. However, we setup HRMAN 2.0 to use the probability maps created by the StarDist CNN to enhance nuclei detection (Figure S1a). With this approach, we could greatly improve segmentation by prevention of over-segmentation

(as is sometimes, the case with water-shedding segmentation), achieve better separation of overlapping or touching nuclei, suppress staining artefacts or correct for uneven fluorescence. In very difficult to segment images, we can still observe segmentation artefacts, but in these cases, we would recommend optimising the experimental and imaging conditions (e.g., cell densities). Again, HRMAN 2.0 can retrieve the trained CNN from a central repository autonomously without the user having to manually load the file.

Similar to StarDist, Cellpose is a generalised cell segmentation method relying on a trained CNN (Stringer et al., 2021). We fully implemented Cellpose within HRMAN 2.0, and it can be used to segment cells of any kind and/or fluorescence stain (Figure S1b). As a generalised model, Cellpose was also able to accurately detect label-

**TABLE 2** System requirements for running HRMAN 2.0

	Minimal	Optimal	Optimal (with GPU acceleration)
System requirements	MacOS 10.12.6/ Windows 7 (or newer) QuadCore CPU >2.0 GHz (e.g., Intel® Core™ i7-7700 or AMD Ryzen™ 3 2200) 8 Gb RAM (e.g., 1600 MHz DDR3) 2 Gb of hard drive storage for KNIME + HRMAN 2.0 and additional storage of about 5 times the size of the image dataset (e.g., 50 Gb for 10 Gb of imaging raw data)	MacOS 10.14.6/Windows 10 Multicore CPU >4.0 GHz (e.g., Intel® Core™ i9-10900 or AMD Ryzen™ 9 5950X) 32 Gb RAM (e.g., 3200 MHz DDR5) 2 Gb of high-speed PCIe 4.0 SSD storage for KNIME + HRMAN 2.0 and additional storage of about 5 times the size of the image dataset (e.g., 50 Gb for 10 Gb of imaging raw data)	Same as optimal but with an additional NVIDIA GPU with at least 4 Gb of GDDR5 VRAM and CUDA 10.0 compatibility (e.g., NVIDIA GTX 1070Ti)
Expected analysis times (60 wells, 15 fields of view each)	<u>Infection analysis:</u> ~2 hr <u>Recruitment analysis:</u> ~6 hr <u>3D-Infection analysis:</u> >1 day <u>3D-Recruitment analysis:</u> >1 day <u>Training novel CNN:</u> Not recommended	<u>Infection analysis:</u> ~1 hr <u>Recruitment analysis:</u> ~3 hr <u>3D-Infection analysis:</u> ~12 hr <u>3D-Recruitment analysis:</u> >1 day <u>Training novel CNN:</u> Not recommended	<u>Infection analysis:</u> ~1 hr <u>Recruitment analysis:</u> ~1.5 hr <u>3D-Infection analysis:</u> ~3 hr <u>3D-Recruitment analysis:</u> ~4 hr <u>Training novel CNN:</u> ~1–7 days (GPU-dependent)

free cells in brightfield images (Figure S1b). We found that this segmentation was versatile enough to segment brightfield images of the yeast *Cryptococcus neoformans* not just mammalian cells for which the algorithm is mainly used (Figure S1b). Impressively, by using Cellpose, HRMAN 2.0 accurately separated densely packed cells, like a confluent monolayer of human foreskin fibroblasts, a common model host cell line in the field of host *Toxoplasma* interaction (Figure S1b). Since running Cellpose is computationally expensive, we recommend using GPU acceleration.

For both the StarDist-enhanced nuclei segmentation and Cellpose-driven cell segmentation, we configured HRMAN 2.0 to allow for the user to choose between the classical (faster) algorithms and these more sophisticated methods, depending on their requirements and capabilities of their computer. In summary, HRMAN 2.0 now offers a full ensemble of state-of-the-art CNN-based instance segmentation methods. These can be used without the user having to write a single line of code.

## 2.4 | 3D analysis

Given the improved segmentation of cells using Cellpose and the option to run it in 3D for z-stacks (Stringer et al., 2021), we were now able to add 3D analysis capability to HRMAN 2.0 (Figure S2). This allows for analysis of imaging screens that use 3D z-stacks for each position. Cellpose is used to detect cells and their connecting labels in all three dimensions, and, at the same time, pathogen segmentation has been updated to allow for detection of corresponding labels in a 3D-stack (Figure S2a). For analysis of this type, users of HRMAN 2.0 need to ensure that their imaging setup, especially the z-step size,

matches the capabilities of their imaging system and the specificities of the fluorescent stains. In this way, we could use HRMAN 2.0 to measure pathogen vacuole volumes instead of areas and therefore improve the sensitivity for pathogen replication and growth quantification. Similarly, we designed HRMAN 2.0 to classify protein recruitment to pathogens independently for each z-plane that the pathogen vacuole was detected in. This improved specificity of the recruitment classification (Figure S2a). To illustrate this new capability of HRMAN 2.0, we used the program to segment a confluent epithelium of A549 cells, which yielded impressive results and shows how HRMAN 2.0 might be used in the future (Figure S2b).

## 2.5 | Improved artificial intelligence recruitment classification

The original HRMAN's greatest innovation was use of deep CNNs for classification of protein recruitment to pathogen vacuoles (Fisch et al., 2019). The original program used the DL4J deep learning framework, which worked reliably, but is slightly outdated now. We therefore replaced the DL4J framework with Keras (Chollet, 2015) using a TensorFlow backend (Abadi et al., 2016), which should future-proof HRMAN 2.0 for the coming years. Importantly, use of Keras allowed us to implement more modern and complex deep CNN architectures and replace the original HRMAlexNet (Fisch et al., 2019; Krizhevsky et al., 2012). HRMAN 2.0 now uses a modified version of ResNet50 (He, Zhang, Ren, & Sun, 2016) for image classification (Figure S3). We have trained a total of six new models for different pathogens and fluorescent stains, which all achieved a classification accuracy >92% (Figure S4a–f). Since HRMAN 2.0 also reports classification

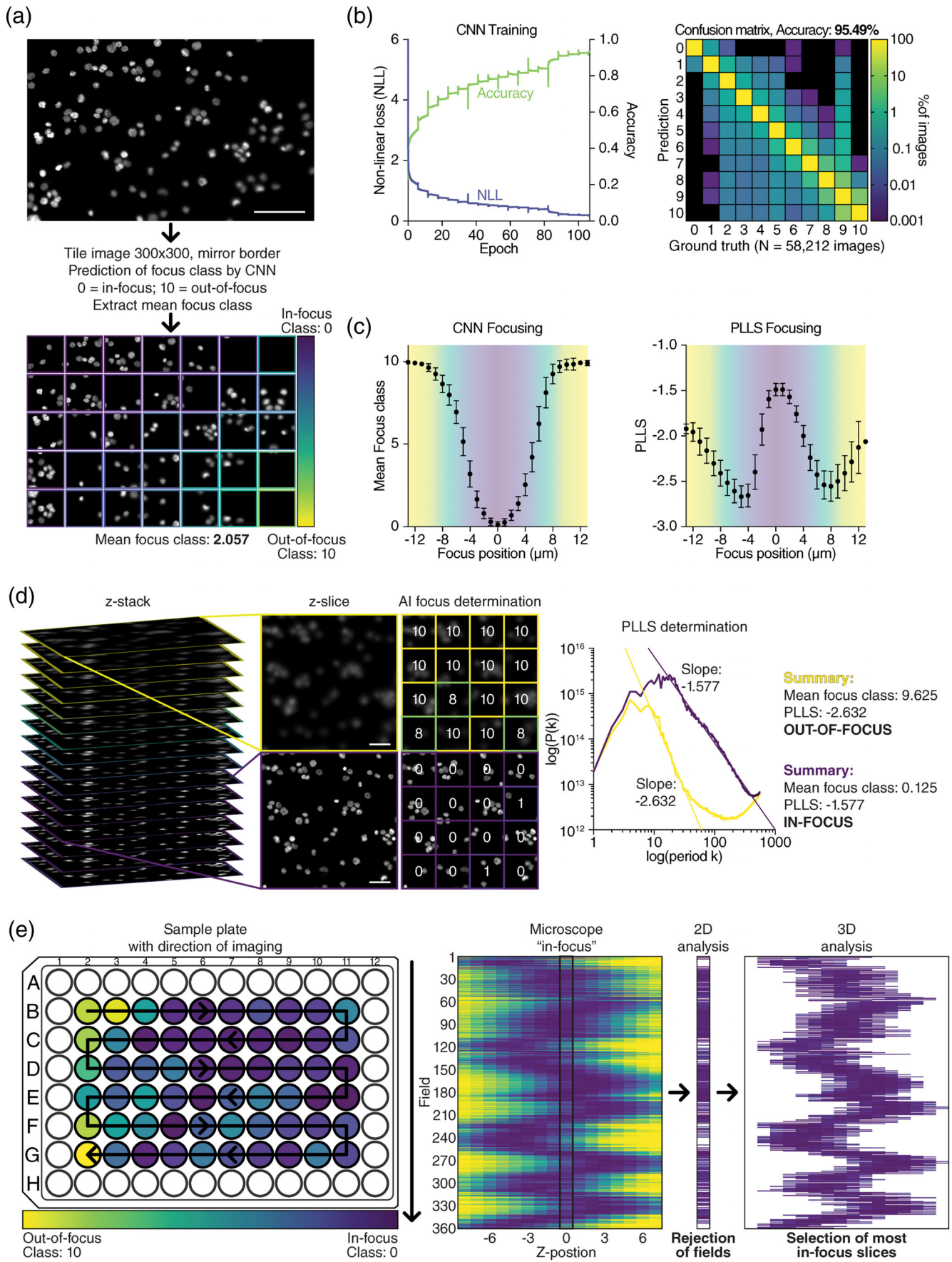


FIGURE 2 Legend on next page.

confidence to the user, analysis can be repeated with a different model, should the user choose to. We also managed to train a generalised recruitment classification model using four different pathogens (*Toxoplasma gondii*, *Salmonella typhimurium*, *Chlamydia trachomatis*, *Cryptococcus neoformans*), more than 10 different fluorescent stains and images from five different automated and non-automated and confocal/widefield microscopes which achieved an overall accuracy of 95.80% (Figure S4c).

Further improvements were achieved by expanding the dataset prior to classification. To do so, we configured HRMAN 2.0 to flip and rotate each image and then run the classification separately for each pathogen vacuole. Following this quintuplicate classification, the mode (i.e., consensus) of classifications for each pathogen vacuole was collected to obtain the final prediction (Figure 3a). In our test dataset, consisting of >100,000 pathogen images, for more than 90% of all pathogen vacuoles, the prediction was unique meaning it remained the same regardless of orientation of the image (Figure 3a). For the majority of the remaining images, the CNN prediction contained two classes (Figure 3a). Importantly, this quintuplicate expansion of the dataset and prediction followed by gathering of the consensus increased accuracy of the generalised model from 95.80% to 98.84% (Figure 3b). We further compared this new type of classification to the old version (using just a single prediction per pathogen vacuole) and observed that for the majority the confidence in prediction was unchanged (Figure 3c). However, the overall confidence increased from 87.3% in the single to 94.9% in the quintuplicate prediction (Figure 3c). In most cases, confidence was improved for pathogen vacuoles that showed a high background, overlapping pathogens or incomplete recruitment and can explain the increased overall accuracy of classification (Figure 3c).

Another innovation in use of the deep CNNs for image classification comes with our introduction of a central repository (Figure 3d). In this way, we designed HRMAN 2.0 to automatically connect to a central database and let users choose which trained model they want to use for their analysis (Figure 3d). Once we or other users have trained a new neural network for use in HRMAN 2.0, this model can be deposited in the repository and is then automatically available to all users of HRMAN 2.0 (Figure 3d).

We furthermore added a second independent workflow to the HRMAN 2.0 analysis suite (Figure 3e). This workflow allows users to create their own annotated datasets and use them for training of custom CNNs for their fluorescent stains/protein recruiting to pathogens inside any host cell (Figure 3e). This all-in-one workflow starts by providing regular fluorescence images, which will then be processed as in HRMAN 2.0. Instead of calculating readouts and performing image quantification, this pipeline creates cropped images and displays them to the user in an interactive annotation tool with which the pathogen inclusion can be classified by the user into recruited/non-recruited/artefact classes (Figure 3e). Ideally, 2,000–5,000 images should be annotated per class (“the more, the better”). Classes should be balanced and contain equal number of example images for training to exclude the possibility of the model skewing into one direction. Once enough images have been annotated, the dataset is partitioned, and the training images are augmented (flip, rotate, translate, zoom, brightness, noise injection, random removal of image parts) to create a sufficiently large image database for training of a good CNN model (Shorten & Khoshgoftaar, 2019). From there, training of the new KERAS ResNet50 architecture-based neural net commences (this step requires use of a GPU), and following successful training the model is saved and the performance is evaluated (Figure 3e). In this way, we provide users with a tool to create their own custom neural networks which can optionally be submitted to the central repository for other users to benefit as well.

To further improve the CNNs used for protein-recruitment classification, we established a project on the Zooniverse platform (<https://www.zooniverse.org>) called “*Microbe Watch*” (<https://www.zooniverse.org/projects/sb99/microbe-watch>). *Microbe Watch* allows us to pursue a community-based approach to improve the accuracy of analysis in HRMAN 2.0. It allows large numbers of specialists and non-specialists to annotate data for training of CNNs (Figure 3f), by establishing a consensus annotation for each image in the dataset thereby reducing bias in training datasets (>130,000 individual annotations for >8,400 images, as of April 20, 2021) (Pelt, 2020). Machine learning algorithms trained using public- and expert-consensus have proven successful and can accurately complete tasks such as image classification in an unbiased manner (Segebarth et al., 2020; Spiers et al., 2020).

**FIGURE 2** Focus quality determination performed by HRMAN 2.0. (a) Illustration of how raw microscopy images (top) are tiled into 300x300 image crops which are then individually classified on their focus quality using the trained convolutional neural network (CNN) with 0 being in focus and 10 being out of focus. The overall focus class of the picture is determined as the mean of the parts. Picture shows nuclei of A549 cells. Scale bar: 100  $\mu\text{m}$ . (b) Learning curve displaying the non-linear loss and accuracy gain of the CNN during training for focus quality judgement (left) and confusion matrix showing performance and accuracy of the obtained CNN model (right). Logarithmic colour scale; black no classification. (c) Graphs illustrating performance of the trained CNN and calculation of the power log-log slope (PLLS) of the pixel intensity spectrum to classify focus quality.  $n = 360$  images for each focus position (27 positions ranging from  $-13$  to  $+13$   $\mu\text{m}$ ). (d) Graphical representation of HRMAN 2.0's focus determination process for images from a z-stack. Two example images, one in-focus (magenta) and one out-of-focus (yellow) highlighted, to illustrate the CNN-based focus classification and determination of the PLLS to then reach the final judgement of focus quality. The AI-based focus-quality judgement (middle) illustrates the individual classes of image tiles as determined by the trained neural network. Graph on the right shows the calculation of the PLLS of the two example images from the z-stack. Scale bar: 50  $\mu\text{m}$ . (e) Graphical illustration of focus determination for a whole multi-well plate. Arrow indicates well/field order during acquisition. HRMAN 2.0 judges focus quality for the whole well and for each image individually (here from z-stacks), as indicated using the colour scale on the plate and the heatmap. Depending on the following analysis type, images are either rejected from a 2D analysis, if they are out-of-focus, or the most in-focus planes are selected for a 3D analysis

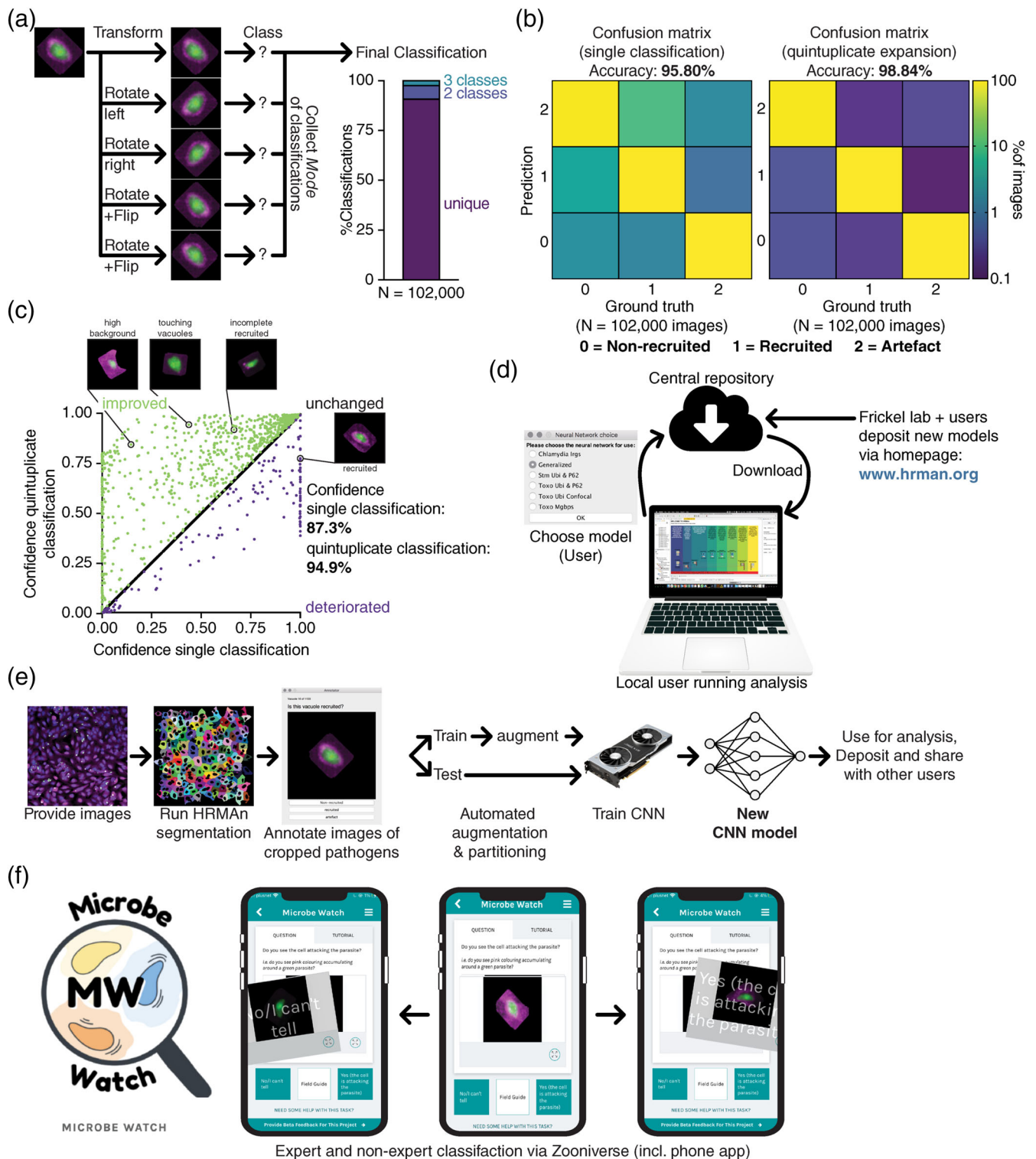


**FIGURE 3** Improvement to the HRMAN 2.0 workflow for protein recruitment classification. (a) Graphical illustration of quintuplicate expansion of the dataset prior to classification for increased accuracy. Classification distribution graph shows a test with  $n = 102,000$  vacuole images. (b) Quintuplicate expansion improves confidence in and accuracy of the classification, as shown in the confusion matrices either using a single prediction (left) or quintuplicate expansion prior to prediction (right) with a generalised model. (c) Comparison of prediction confidences for protein recruitment to pathogen vacuoles using a single prediction or using quintuplicate expansion prior to prediction. Overall confidence improved, especially for images that are hard to classify (high background, touching vacuoles, incomplete recruitment, see highlighted examples). (d) Illustration of the newly implemented central repository for trained CNN model for protein recruitment classification. (e) Steps of the second workflow in the HRMAN 2.0 ensemble that allows users to train their own convolutional neural networks (CNN). This workflow handles images like the HRMAN 2.0 analysis pipeline but then allows users to annotate their newly created training images and directly feed them into a training routine also providing the naïve architecture of the KERAS ResNet50 as used by HRMAN 2.0. (f) “Microbe Watch” Zooniverse project for annotation of vacuole images online or within a mobile phone app

## 2.6 | New example analysis applications

HRMAN was able to accurately quantify host–pathogen interactions on a high-throughput scale and computed more than 15 comprehensive readouts. We have illustrated this before (Fisch et al., 2019), and HRMAN 2.0 produces the same readouts (Figure 1c), although faster and even more precisely. We therefore want to showcase more possible applications of HRMAN 2.0 and also demonstrate its usability for pathogens other than *T. gondii* or *Salmonella*.

HUVECs are known to kill Tg by directly acidifying the vacuoles (Clough et al., 2016). HRMAN 2.0 was therefore deployed to classify vacuoles based on LysoTracker signal (Figure 4a), which revealed a significant increase in the percentage of acidified vacuoles upon treatment with 250 IU/ml IFN $\gamma$  (Figure 4a). Furthermore, HRMAN 2.0 was able to show that Tg parasites in acidified PVs stop replicating as indicated by a reduced average size when compared to non-acidified PVs (Figure 4a).

Differences between type I and type II parasites include the recruitment of mitochondria to the PV. Type I Tg expresses a protein called MAF1, which recruits mitochondria (Figure 4b) and aids in parasite modulation of the host immune response (Pernas et al., 2014). HRMAN 2.0 was able to reproduce these observations, when analysing MitoTracker fluorescence intensity around type I or type II PVs (Figure 4b).

HRMAN 2.0 can also be used to examine the effects of pathogen-derived virulence proteins, instead of focusing on questions derived from host defence mechanisms. Type II Tg is known to express and secrete the dense granule protein GRA15 which accumulates at the PV membrane and leads to induction of NF $\kappa$ B signalling (Rosowski et al., 2011). Using the protein localization analysis pre-configuration, HRMAN 2.0 was able to measure the mean fluorescence of immune-stained p65 signal in the host cell cytosol and the host cell nucleus and calculate the ratio (Figure 4c). p65 accumulation in the nucleus is a sign for NF $\kappa$ B activation (Gillmore, 2006). Comparing WT and  $\Delta$ GRA15 Tg infection of HFFs, HRMAN 2.0 could show that the strength of NF $\kappa$ B activation directly correlated with the number of vacuoles per cell (Figure 4c).

Robust segmentation of host cells, host cell nuclei and pathogens is the backbone of HRMAN 2.0's analysis strength. Since all parameters used for this segmentation can be changed, for example, the thresholding method, image normalisation and saturation or filter values, it is easy to adapt HRMAN 2.0 to work with different pathogens. First, we trained HRMAN to be capable of working with *C. trachomatis* (Ctm) infected cells. Ctm forms reticulate structures in the cytosol, known as inclusion bodies (IBs) (Elwell, Mirrashidi, & Engel, 2016). These can vary in size significantly, but HRMAN 2.0 was nonetheless able to accurately segment the IBs (Figure 4d). We then used this segmentation and re-trained the CNN to classify recruitment of murine Irg proteins (Figure S4b). Irgs play a crucial role in the defence against Ctm in murine cells (Pilla-Moffett, Barber, Taylor, & Coers, 2016), and using high-throughput image analysis, HRMAN 2.0 could show that mIrgB6 accumulated at Ctm inclusion bodies in an IFN $\gamma$ - and mIrgM-dependent manner in MEF cells of different genetic backgrounds (Figure 4d).

Another pathogen commonly infecting macrophages is *C. neoformans* (Srikanta, Santiago-Tirado, & Doering, 2014). This fungus grows as a unicellular yeast and replicates within cells by budding (May, Stone, Wiesner, Bicanic, & Nielsen, 2016; Rudman, Evans, & Johnston, 2019). A number of GFP-tagged wildtype (Bielska et al., 2018; Voelz, Johnston, Rutherford, & May, 2010) and virulence factor knockout (Evans et al., 2019) *Cryptococcus* strains are available which make high content imaging possible. Alternatively, fungi can also readily be stained with the fluorescent dye calcofluor white. Re-training HRMAN to recognise intracellular *Cryptococcus* and using the decision tree ML algorithm to classify budding, and thus replicating, fungi (they appeared distinctively larger and with lower circularity), revealed that IFN $\gamma$ -treated human THP-1 cells were able to restrict the growth of this pathogen (Figure 4e).

With the exception of viruses, we demonstrated that HRMAN 2.0 was able to work with any kind of intracellular pathogen, irrespective of being bacteria, protozoans or fungi. Importantly, re-training HRMAN only took little time, but resulted in a robust analysis pipeline that can be used for many future experiments. All pre-set filters for the different pathogens are available to users of HRMAN 2.0.

## 3 | DISCUSSION

Advances in computational hardware and software developments have made deep CNNs a powerful image analysis tool (LeCun, Bottou, Bengio, & Haffner, 1998; Russakovsky et al., 2015). CNNs are able to generalise patterns independent of minor phenotypic differences and allow for a more robust classification of images or parts thereof (LeCun et al., 2015). Automated image analysis programs, some of which incorporate machine learning elements, have been developed and are successfully used for classical image segmentation (Osaka et al., 2012), but when presented with the problem of classifying host protein recruitment to a pathogen, inaccurate classical image segmentation could lead to erroneous results (Pärnamaa & Parts, 2017). HRMAN 2.0 circumvents these problems and delivers user-defined automated and unbiased enumeration.

In recent years, many programs have been developed that make use of computer vision advances to drive scientific progress in basic research (Eulenberg et al., 2017; Pärnamaa & Parts, 2017) and in application in the clinic (Cireşan, Giusti, Gambardella, & Schmidhuber, 2013; Esteva et al., 2017; Litjens et al., 2017; Roth et al., 2018). For microscopy image analysis, these usually are focused on one step, for example, image reconstruction from super-resolution imaging (Ouyang, Aristov, Lelek, Hao, & Zimmer, 2018; Weigert et al., 2018), segmentation of nuclei or cells (Ronneberger, Fischer, & Brox, 2015; Schmidt et al., 2018; Stringer et al., 2021) or classification of image parts (Falk et al., 2019). While we did not invent novel ways of analysing images with CNNs, HRMAN 2.0 delivers a unique ensemble of pre-trained networks, combining the power of these individual solutions. Following the initial publication of HRMAN and application for host *Toxoplasma* interaction, similar approaches have been made for quantification of host *Plasmodium* interaction (Davidson

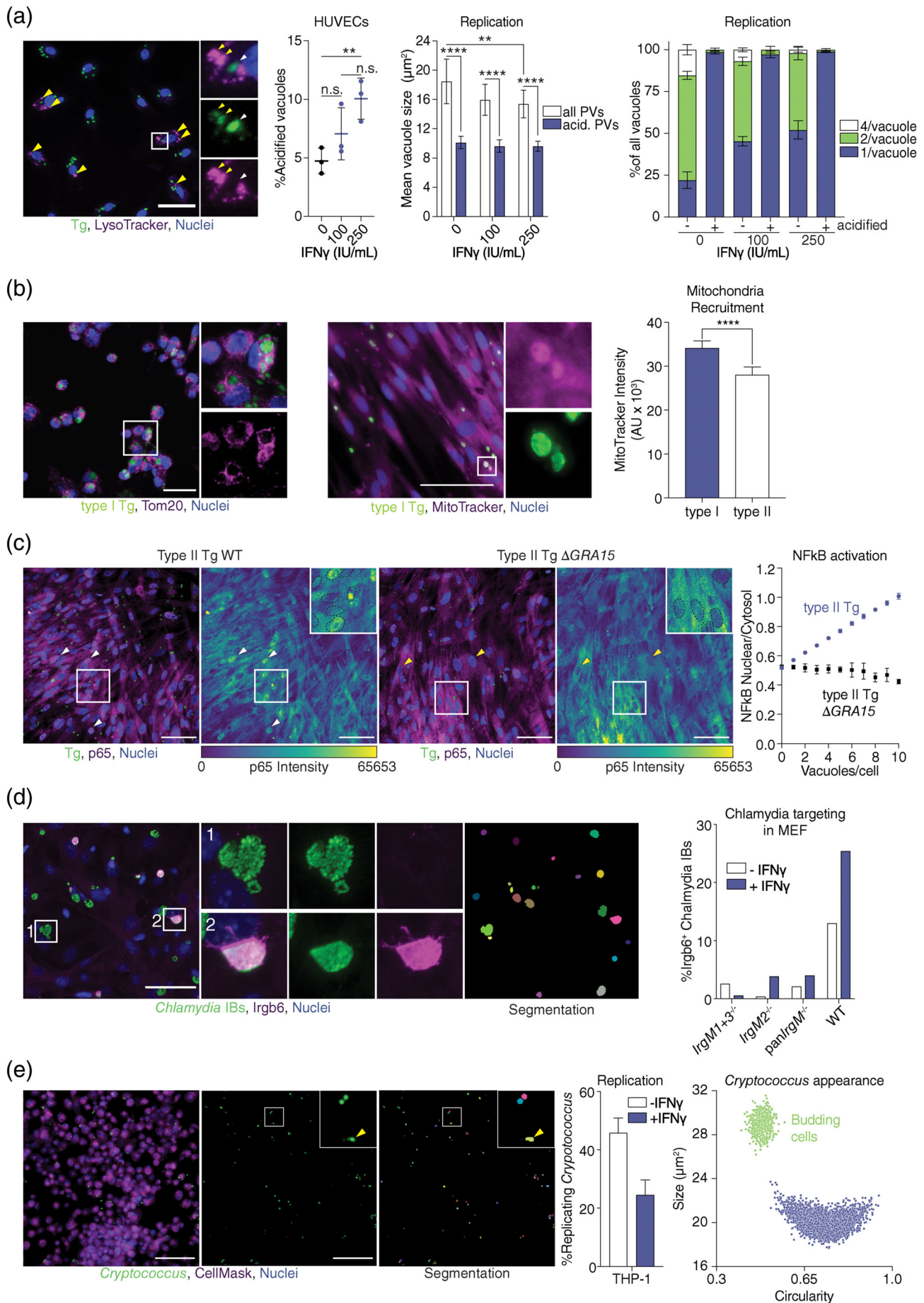


FIGURE 4 Legend on next page.

et al., 2021; Hung et al., 2020). With the release of HRMAN 2.0, we now deliver a program with broad applicability to host–pathogen interactions in general. We designed HRMAN 2.0 with a focus on intracellular pathogens and the interaction with their host cell. Given HRMAN's flexibility, extracellular pathogens prior to entry into the host cell can be analysed, too. Experimental setup and appropriate readouts can be tailored to pathogens outside host cells. For instance, staining of extracellular pathogens prior to permeabilisation of imaging specimens could be used to assess the invasion rate of the pathogen. However, we need to point out that although HRMAN 2.0 is a versatile program, it is focused on host–pathogen interaction analysis and is therefore not the “swiss army knife” of general image analysis or for high-throughput imaging, where programs like ImageJ/FIJI (Schindelin et al., 2012) and CellProfiler (Carpenter et al., 2006) have their strengths, respectively.

The combination of automated image segmentation, decision tree ML and another deep CNN for quantification makes HRMAN 2.0 a powerful and user-friendly program for analysis of host–pathogen interaction at the single-cell level. HRMAN 2.0 is capable of detecting and quantifying multiple pathogen and host parameters, as illustrated with several pathogens of varying sizes and growth morphologies. Designed for biologists, HRMAN 2.0 requires no coding or specialised computer science knowledge. The modular architecture and graphical representation of the analysis pipeline, provided by the use of KNIME Analytics platform (Berthold et al., 2008), allows users to tailor experimental outputs to their own datasets and questions. Thus, HRMAN 2.0 can be rapidly applied to many similar large-scale, imaging experiments. Similarly, HRMAN 2.0 can also be used to answer questions that do not directly derive from host–pathogen interactions, but from the pathogen's biology itself. As mentioned above, with elegant

staining strategies and experiment design, HRMAN 2.0's analysis capabilities can enable users to assess invasion rates and extracellular behaviour of pathogens. Furthermore, using higher-resolution imaging, HRMAN 2.0 could be used to quantify the morphology of pathogens within vacuoles or for example chronic forms of pathogens such as the *Toxoplasma* bradyzoite cyst, which are planned for the next updates of HRMAN. As such, HRMAN 2.0 will allow a broad range of researchers to extend into the realm of high-throughput single-cell analysis of host–pathogen interaction.

HRMAN 2.0 includes performance improvements and provides users with an even more precise image analysis tools. One major new improvement was the extension of HRMAN 2.0 from a simple 2D, or z-projected analysis to the three-dimensional space. Measuring volumes instead of areas is especially useful for quantification of pathogen growth and the prediction of replication using decision tree ML. High-throughput 3D analysis therefore promises to reveal even more subtle phenotypes that would have been missed by manual enumeration of microscopy slides. Similarly, HRMAN will also be updated to work with time-resolved image sequences from live-imaging experiments in the future. Tracking intracellular pathogens and the respective host cells over time would enable grouping cells and/or pathogens into subsets based on their fate, that is, growth, persistence or killing (Fazeli et al., 2020). Making use of many excellent algorithms for tracking of motile and immotile cells, for example, TrackMate (Tinevez et al., 2017), will be useful for this. The culmination of these two analysis types would be time-resolved 3D image analysis, which at present is restricted mainly by computational limitations and dataset sizes.

Other improvements of HRMAN 2.0 were derived from the rapidly evolving field of computer vision. The original HRMAN relied on

**FIGURE 4** New application of HRMAN 2.0 for analysis of host–pathogen interactions. (a) Left: Representative image of IFN $\gamma$ -primed human umbilical-vein endothelial cells (HUVEC) cells, infected with type II *Toxoplasma gondii* (Tg) for 4 hr and stained with LysoTracker. Cropped images show Tg in acidified vacuoles (yellow arrowheads) and non-acidified vacuoles (white arrowheads). Green: Tg; Magenta: LysoTracker; Blue: Nuclei. Scale bar 30  $\mu$ m. Middle: HRMAN 2.0 quantification of the proportion of acidified Tg vacuoles in respect to different concentrations of IFN $\gamma$  used for priming at 4 hr p.i. and Right: Comparison of Tg growth in acidified versus non-acidified vacuoles as measured by the mean vacuole size and proportion of vacuoles containing the indicated number of parasites at 12 hr p.i. (b) Left: Representative immunofluorescence image of type I (RH) Tg infected human THP-1 cells at 24 hr p.i. and stained with mitochondria marker Tom20. Middle: Type I (RH) Tg infected human foreskin fibroblasts (HFFs) at 8 hr p.i. and stained with MitoTracker. Insets show recruitment of host cell mitochondria to the Tg vacuole. Green: Tg; Magenta: Tom20/MitoTracker; Blue: Nuclei. Scale bar 50  $\mu$ m. Right: HRMAN quantification of MitoTracker radial fluorescence intensity surrounding vacuoles of type I or type II Tg at 8 hr p.i. (c) Left: Representative immunofluorescence image and intensity maps of human foreskin fibroblasts (HFF) infected with type II Tg WT or  $\Delta$ GRA15 for 6 hr and stained for p65. White arrowheads indicate examples of accumulation of p65 in the host cell nucleus of cells infected with type II Tg WT and yellow arrowheads indicate nuclei without p65 accumulation in cells infected with type II Tg  $\Delta$ GRA15. Insets depict higher magnification with nuclei outlined by the dotted line. Green: Tg; Magenta: p65; Blue: Nuclei. Scale of intensity map indicated below. Scale bars 50  $\mu$ m. Right: HRMAN 2.0 quantification of the ratio between nuclear and cytosolic p65 fluorescence signal and correlation with the number of Tg vacuoles per cell for type II Tg WT or  $\Delta$ GRA15 infected HFFs. (d) Left: Example immunofluorescence image and automated segmentation of *Chlamydia trachomatis* inclusion bodies (IB) in infected and IFN $\gamma$ -treated mouse embryonic fibroblasts (MEF) stained for IrgB6. Inset 1 shows an IB without and inset 2 with IrgB6 recruitment. Green: *Chlamydia* IBs; Magenta: IrgB6; Blue: Nuclei. Scale bar 30  $\mu$ m. Right: Automated HRMAN classification and quantification of IrgB6 recruitment to *Chlamydia* IBs in naïve or IFN $\gamma$ -primed MEF cells of indicated genetic backgrounds. (e) Left: Example immunofluorescence image and automated segmentation of *Cryptococcus* from IFN $\gamma$ -treated, PMA-differentiated THP-1 cells stained with CellMask. Insets highlight image and segmentation of a budding *Cryptococcus* cell (yellow arrowheads). Green: *Cryptococcus*; Magenta: CellMask; Blue: Nuclei. Scale bar 300  $\mu$ m. Right: Automated HRMAN quantification of *Cryptococcus* replication and scatter plot depicting *Cryptococcus* appearance and budding detection in naïve or IFN $\gamma$ -primed THP-1 cells at 10 hr p.i. **Data information:** Graphs in (a–c) and (e) from  $n = 3$  independent experiments  $\pm$  SEM and in (d) from  $n = 1$  proof-of-principle experiment. \*\* $p \leq .01$ ; \*\*\*\* $p \leq .0001$  in (a) from two-way ANOVA following adjustment for multiple comparisons and in (b) from unpaired  $t$  test; n.s., not significant

the DeepLearning4J library, but newer libraries like Keras and TensorFlow (Abadi et al., 2016; Chollet, 2015) now deliver better deep CNNs, that train faster and classify images with ever increasing accuracy (Nichols, Herbert Chan, & Baker, 2019). HRMAN 2.0, at this time, is the only program for analysis of host–pathogen interactions that makes use of powerful trained CNNs in every step of the analysis (image quality assessment, object detection, image classification and phenotype quantification). While for each of these problems, CNN-based algorithms have been created as a solution individually (Krizhevsky et al., 2012; Pärnamaa & Parts, 2017; Schmidt et al., 2018; Stringer et al., 2021; Yang et al., 2018), HRMAN 2.0 combines them into a single turnkey analysis pipeline. Alongside classical image analysis stemming from signal theory, a custom CNN is provided for focus quality control. Another application of deep CNNs within HRMAN 2.0 is instance segmentation. This computer vision task involves prediction of object instances and their per-pixel masks. Both StarDist and Cellpose now allow high-precision detection of nuclei and host cells, respectively (Schmidt et al., 2018; Stringer et al., 2021). Replacing the classic segmentation approach with deep CNNs made segmentation more reliable and robust. This will help HRMAN 2.0 to cope with a wide array of sample preparations and imaging protocols without requiring additional user intervention. Importantly, HRMAN 2.0, as a turnkey analysis pipeline, facilitates use of these elegant methods, by not requiring the user to adapt them for their specific dataset. Lastly, the previously implemented CNN for protein-recruitment analysis (Fisch et al., 2019) has been updated and classification accuracy greatly improved using a newer CNN architecture and quintuplicate expansion of the datasets. We also established the Zooniverse project “Microbe Watch” with which we are gathering large numbers of consensus annotations to train CNNs for protein recruitment prediction that are not biased by annotation from a single user. This annotation bias is a known problem for training of CNNs (Pelt, 2020) and by gathering millions of annotations for thousands of images the next CNNs for HRMAN 2.0 should deliver no or little bias. Finally, the newly implemented central repository for trained deep CNN models will facilitate exchange between different users and make sure that HRMAN 2.0 can always access the latest developments.

Taken together, HRMAN 2.0 is a useful tool for research and a scaffold for future improvements that promise to elevate the level of automation and intelligence even further. Thus, HRMAN 2.0 has the potential to become an integral analysis tool for the host–pathogen interaction research community.

## 4 | EXPERIMENTAL PROCEDURES

### 4.1 | Cell, parasite and bacteria culture

THP-1 (TIB-202, ATCC, Male cell line, RRID:CVCL\_0006) were maintained in RPMI with GlutaMAX (Gibco) and 10% heat-inactivated FBS (Sigma). THP-1 cells were differentiated with 50 ng/ml phorbol 12-myristate 13-acetate (PMA, P1585, Sigma) for 3 days followed by

a rest for 2 days in complete medium without PMA. HeLa (ECACC, Sigma, Female cell line, RRID:CVCL\_0030), A549 lung epithelial cells (CCL-185, ATCC, Male cell line RRID:CVCL\_0023), mouse embryonic fibroblasts (MEF) and human foreskin fibroblasts (HFF, Male cell line, RRID:CVCL\_XB54) were maintained in DMEM with GlutaMAX (Gibco) supplemented with 10% FBS. Cells were not used beyond passage 20. Human umbilical vein endothelial cells, HUVECs, (C12203, Promocell), were maintained in M199 medium (Gibco) supplemented with 30 µg/ml endothelial cell growth supplement (ECGS, 02–102, Upstate), 10 units/ml heparin (H-3149, Sigma) and 20% FBS (Sigma). Cells were grown on plates, pre-coated with 1% (w/v) porcine gelatin (G1890, Sigma). HUVEC were not used beyond passage 6. Primary MEFs were obtained by digesting E12.5–14.5 embryos in 0.25% trypsin (Gibco) and then passaged in Dulbecco's Modified Eagle's Medium (Gibco) supplemented with 10% heat-inactivated FBS (Sigma).

Tg expressing luciferase/eGFP (RH type I and Prugniaud [Pru] type II) were maintained by serial passage on monolayers of HFF cells in DMEM with GlutaMAX (Gibco) supplemented with 10% FBS. *C. trachomatis* LGV-L2 was propagated in Vero monkey kidney cells.

All cells were regularly tested for mycoplasma contamination, cultured without addition of antibiotics and grown at 37°C in 5% CO<sub>2</sub> atmosphere. Cells were stimulated for 16 hr prior to infection in complete medium at 37°C with addition of 50 IU/ml human IFN $\gamma$  (285-IF, R&D Systems).

### 4.2 | *Cryptococcus* culture and infection

*Cryptococcus* strain H99-GFP (Voelz et al., 2010) was grown from frozen cultures onto YPD agar (Merck Sigma Aldrich) plates at 25°C overnight. The day before infection (Day 1) a subculture was made from the stock plate into 2 ml YPD broth (Merck Sigma Aldrich). Subcultures were grown overnight at 25°C with constant shaking. On the day of infection (Day 2), 500 µl of *Cryptococcus* overnight culture was washed twice with PBS and re-suspended in 100 µl human serum (S4190, Biowest). *Cryptococcus* cells were counted with a haemocytometer, and the required volume was added to a second tube to give the desired MOI (see below) and made up to final volume with fresh human serum (20 µl final volume required per well of a 96-well plate). Tubes were incubated for 1 hr at room temperature for serum opsonisation to occur.

Forty eight hours before the day of infection (Day 0), THP-1 cells were cultured, seeded, differentiated (1 day only) and treated with IFN $\gamma$  as described above. Cells were seeded at  $3.2 \times 10^4$  cells per well into 96-well imaging plates (655090, Greiner).

On the day of infection (Day 2), THP-1 cells were infected with human serum opsonised *Cryptococcus* at an MOI of 1.5 by adding 20 µl of human serum containing *Cryptococcus* suspension to each well.

Infected plates were incubated for 2 hr and then washed twice with PBS to remove extracellular *Cryptococcus* cells, and medium was replaced with IFN $\gamma$  added for appropriate treatment conditions. Cells were fixed with 4% formaldehyde for 15 min at desired timepoints,

washed twice with PBS, and then stained with Cell mask/Hoechst as described below for imaging.

### 4.3 | *Chlamydia* infection and imaging

Primary MEFs were plated onto glass cover slips and infected with *C. trachomatis* at an MOI of 1 by centrifugation at 3000 rpm at 4°C for 30 min. Twelve hours post-infection, infected cells were treated with 100 µl IFN $\gamma$ . At 20 hr post-infection, cells were washed three times with PBS (Gibco) prior to fixation in ice cold methanol for 5 min. Fixed cells were blocked with 2.5% (w/v) BSA (Equitech-Bio Inc) in PBS for 30 min at room temperature. Blocked cells were incubated with primary antibodies in 2.5% BSA-PBS for 1 hr at room temperature, washed three times with PBS, and then incubated with Alexa Fluor-conjugated secondary antibodies (Molecular Probes) as well as Hoechst 33258 diluted in 2.5% BSA-PBS for 1 h at RT. Stained cover slips were mounted onto glass slides with a solution of 90% Mowiol and 10% phenylenediamine. Samples were imaged using a Zeiss Axio Observer Z1 inverted phase contrast fluorescence microscope.

### 4.4 | *Toxoplasma* infection

Parasites were passaged the day before infection. Tachyzoites were harvested from HFFs by scraping and syringe lysis through a 25 G needle. The obtained suspension was cleared by centrifugation at 50g for 5 min and the parasites pelleted by subsequent centrifugation of the supernatant at 550g for 7 min. Tg-containing pellets were washed with complete medium once and finally re-suspended in fresh medium. Viable parasites were counted with trypan blue and used for infection at a multiplicity of infection (MOI) of 1. Infection was synchronised by centrifugation at 500g for 5 min. Two hours after infection, extracellular Tg were removed by washing with PBS three times.

### 4.5 | High-throughput imaging

For simple infection analysis, 50,000 THP-1 cells were seeded per well of a 96-well imaging plate, differentiated and treated as described above. HFFs were harvested by washing a confluent monolayer with PBS and subsequent lifting of the cells with 0.05% trypsin-EDTA (15400054, Gibco). Cells were centrifuged at 250g for 5 min, re-suspended in fresh medium and 20,000 HFFs per well were seeded the day before IFN $\gamma$  treatment. Similarly, HUVECs were harvested, and 15,000 cells per well were seeded in complete medium the day before IFN $\gamma$  treatment. A549s and HeLa cells were harvested in the same way, and 8,000 cells per well were seeded the morning before IFN $\gamma$  treatment. All cells were seeded on 1% (w/v) porcine gelatin (G1890, Sigma) pre-coated black wall, clear bottom 96-well plates (Thermo Scientific). To grow A549 cells into an epithelium-like structure, the cells were allowed to grow fully confluent for 5 days. Cells were treated and Tg-infected as described above. Following fixation

with 4% methanol-free formaldehyde (28906, Thermo Scientific), specimens were permeabilised with PermQuench buffer for 30 min at room temperature. Then PermQuench buffer containing 1 µg/ml Hoechst 33342 and 2 µg/ml CellMask™ Deep Red plasma membrane stain (C10046, Invitrogen) was added, and samples were incubated at room temperature for 1 hr. After staining, the specimens were washed with PBS five times and kept in 200 µl PBS per well for imaging.

For recruitment analysis, the cells were prepared as described above, but they were seeded on 1% (w/v) porcine gelatin pre-coated black wall, glass bottom 96-well imaging plates CG 1.0 (130-098-264, MACS Miltenyi) to allow higher resolution imaging. After fixation, cells were permeabilised identically and then stained with primary antibody (p62, ab56416, Abcam; Ubiquitin FK2, PW8810, Enzo Life Sciences; IRGB6, home-made [Traver et al., 2011]; p65, sc-8008, santa cruz; Tomm20, ab56783, abcam) diluted in PermQuench buffer for 1 hr at room temperature. After three washes with PBS, cells were incubated with the appropriated fluorescently labelled secondary antibody and 1 µg/ml Hoechst 33342 diluted in PermQuench buffer for another hour at room temperature. Then, the specimens were washed with PBS 5 times and kept in 200 µl PBS per well for imaging.

Staining of cells with LysoTracker Red DND99 (L7528, Thermo-Fisher) was performed by adding 50 nM LysoTracker 60 min prior to fixation. Similarly, MitoTracker Red CMXRos (M7512, Invitrogen) was added at 100 nM 30 min prior to fixation.

For simple infection analysis, 96-well plates were imaged on an ArrayScan™ Vtl Live High Content Imaging Platform (Thermo Scientific), a Cell Insight CX7 High-Content Screening Platform (Thermo Scientific) or a Celldiscoverer 7 (Zeiss) using 20 $\times$  magnification and depending on the experiment, 15–20 fields of view per well. For recruitment analysis, plates were imaged on an ArrayScan™ Vtl Live High Content Imaging Platform (Thermo Scientific) or an Opera Phenix High-Content Screening System (Perkin Elmer) but using 40 $\times$ /60 $\times$  magnification and depending on the experiment, 25–50 fields of view per well. In both cases, following image acquisition, the images were exported from HCS Studio Cell Analysis, Zeiss Zen or Perkin Elmer Harmony Software as single channel .tiff files before they were fed into the HRMAN analysis pipeline. 3D rendering of A549 epithelia segmentations was performed using Imaris 8.3.1.

### 4.6 | Data handling and statistics

Data were plotted using Prism 9.0.0 (GraphPad Inc.) and presented as means of experiments as indicated (with usually three technical repeats within each experiment) with error bars as SEM, unless stated otherwise. Significance of results was determined by non-parametric one-way ANOVA or unpaired *t* test as indicated in the figure legends. Benjamini, Krieger and Yekutieli false-discovery rate ( $Q = 5\%$ ) based correction for multiple comparisons as implemented in Prism was used when making more than three comparisons.

All open-source KNIME workflows used in this work can be found at: <https://github.com/HRMAN-Org/HRMAN> and on the homepage [hrman.org](http://hrman.org) under GPLv3 open-source software license. The trained

CNN models and their respective weights obtained through training are deposited on GitHub, the homepage and can be directly obtained within HRMAN 2.0 from the central repository.

## ACKNOWLEDGMENTS

The authors would like to thank Samuel J. Yang (Google Accelerated Science team) for his input on use of deep CNNs for focus detection. We would also like to acknowledge the contribution of Artur Yakimovich (Roche & Artificial Intelligence for Life Sciences CIC) to setting up the initial image classification HRMAlexNet in the original HRMAN and his continued support of the project. Furthermore, we would like to thank Hanna Zafar and Elizabeth R. Ballou (both University of Birmingham) for providing images of extracellular *Cryptococcus* as well as Midori Ishii Kanazawa and Bungo Akiyoshi (both University of Oxford) for providing images of fluorescently labelled *Trypanosoma*. This research was funded, in whole or in part, by The Wellcome Trust. A CC BY license is applied to the AAM arising from this submission, in accordance with the grant's open access conditions. EMF is supported by a Wellcome Trust Senior Research Fellowship (217202/Z/19/Z). This work was supported by the Francis Crick Institute, which receives its core funding from Cancer Research UK (FC001076 to EMF), the UK Medical Research Council (FC001076 to EMF) and the Wellcome Trust (FC001076 to EMF). DF was supported by a Boehringer Ingelheim Fonds PhD fellowship.

## CONFLICT OF INTEREST

The authors declare no conflict of interest.

## AUTHOR CONTRIBUTIONS

**Daniel Fisch, Robert Evans and Eva-Maria Frickel:** Conceived the idea for this work. **Daniel Fisch and Robert Evans:** Performed experiments and worked on software development. **Barbara Clough, Will M. Channell and Jacob Dockterman:** Provided essential experimental protocols and performed experiments. **Sophie K. Byrne:** Created the "Microbe Watch" project on Zooniverse. **Daniel Fisch, Robert Evans and Eva-Maria Frickel:** Analysed and interpreted the data and wrote the article. All authors revised the article.

## DATA AVAILABILITY STATEMENT

All open-source HRMAN 2.0 workflows as well as the models and their respective weights obtained through training can be found at: <https://github.com/HRMAN-Org/HRMAN> and on the homepage <https://hrman.org/> under GPLv3 open-source software license. All image datasets used to train the neural networks in this study are available upon request.

## ORCID

Daniel Fisch  <https://orcid.org/0000-0002-8155-0367>

Eva-Maria Frickel  <https://orcid.org/0000-0002-9515-3442>

## REFERENCES

- Abadi, M., Barham, P., Chen, J., Chen, Z., Davis, A., Dean, J., ... Zheng, X. (2016). TensorFlow: A system for large-scale machine learning. In *12th USENIX Symposium on Operating Systems Design and Implementation (OSDI 16)* (pp. 265–283). Savannah, GA: USENIX Association.
- Berthold, M. R., Cebon, N., Dill, F., Gabriel, T. R., Kötter, T., Meirl, T., ... Wiswedel, B. (2008). KNIME: The Konstanz information miner. In *Data analysis, machine learning and applications. Studies in classification, data analysis, and knowledge organization* (pp. 319–326). Berlin, Heidelberg: Springer.
- Bielska, E., Sisquella, M. A., Aldeieg, M., Birch, C., O'Donoghue, E. J., & May, R. C. (2018). Pathogen-derived extracellular vesicles mediate virulence in the fatal human pathogen *Cryptococcus gattii*. *Nature Communications*, 9, 1–9.
- Bray, M. A., Fraser, A. N., Hasaka, T. P., & Carpenter, A. E. (2012). Workflow and metrics for image quality control in large-scale high-content screens. *Journal of Biomolecular Screening*, 17, 266–274.
- Brodin, P., & Christophe, T. (2011). High-content screening in infectious diseases. *Current Opinion in Chemical Biology*, 15, 534–539.
- Caicedo, J. C., Roth, J., Goodman, A., Becker, T., Karhohs, K. W., Broisin, M., ... Carpenter, A. E. (2019). Evaluation of deep learning strategies for nucleus segmentation in fluorescence images. *Cytometry Part A*, 95, 952–965.
- Carpenter, A. E., Jones, T. R., Lamprecht, M. R., Clarke, C., Kang, I. H., Friman, O., ... Sabatini, D. M. (2006). CellProfiler: Image analysis software for identifying and quantifying cell phenotypes. *Genome Biology*, 7, R100.
- Chollet, F. (2015). *Keras*. Retrieved from <https://keras.io>
- Ciresan, D. C., Giusti, A., Gambardella, L. M., & Schmidhuber, J. (2013). Mitosis detection in breast cancer histology images with deep neural networks. In *Lecture notes in computer science (including subseries lecture notes in artificial intelligence and lecture notes in bioinformatics)* (pp. 411–418). Berlin, Heidelberg: Springer.
- Clough, B., Wright, J. D., Pereira, P. M., Hirst, E. M., Johnston, A. C., Henriques, R., & Frickel, E.-M. (2016). K63-linked ubiquitination targets *Toxoplasma gondii* for endo-lysosomal destruction in IFN $\gamma$ -stimulated human cells. *PLoS Pathogens*, 12, e1006027.
- Davidson, M. S., Yahiya, S., Chmielewski, J., O'donnell, A. J., Gurung, P., Jeniga, M., ... Baum, J. (2021). Automated detection and staging of malaria parasites from cytological smears using convolutional neural networks. *medRxiv*. Retrieved from <https://doi.org/10.1101/2021.01.26.21250284>
- Elwell, C., Mirrashidi, K., & Engel, J. (2016). Chlamydia cell biology and pathogenesis. *Nature Reviews. Microbiology*, 14, 385–400.
- Esteva, A., Kuprel, B., Novoa, R. A., Ko, J., Swetter, S. M., Blau, H. M., & Thrun, S. (2017). Dermatologist-level classification of skin cancer with deep neural networks. *Nature*, 542, 115–118.
- Eulenberg, P., Köhler, N., Blasi, T., Filby, A., Carpenter, A. E., Rees, P., ... Alexander Wolf, F. (2017). Reconstructing cell cycle and disease progression using deep learning. *Nature Communications*, 8, 1–6.
- Evans, R. J., Pline, K., Loynes, C. A., Needs, S., Aldrovandi, M., Tiefenbach, J., ... Johnston, S. A. (2019). 15-keto-prostaglandin E2 activates host peroxisome proliferator-activated receptor gamma (PPAR $\gamma$ ) to promote *Cryptococcus neoformans* growth during infection. *PLoS Pathogens*, 15, e1007597.
- Falk, T., Mai, D., Bensch, R., Çiçek, Ö., Abdulkadir, A., Marrakchi, Y., ... Ronneberger, O. (2019). U-net: Deep learning for cell counting, detection, and morphology. *Nature Methods*, 16, 67–70.
- Fazeli, E., Roy, N. H., Follain, G., Laine, R. F., von Chamier, L., Hänninen, P. E., ... Jacquemet, G. (2020). Automated cell tracking using StarDist and TrackMate. *F1000Research*, 9, 1279.
- Fisch, D., Yakimovich, A., Clough, B., Mercer, J., & Frickel, E.-M. (2020). Image-based quantitation of host cell–*Toxoplasma gondii* interplay using HRMAN: A host response to microbe analysis pipeline. In *Toxoplasma gondii: Methods and protocols* (pp. 411–433). New York, NY: Humana.
- Fisch, D., Yakimovich, A., Clough, B., Wright, J., Bunyan, M., Howell, M., ... Frickel, E. (2019). Defining host–pathogen interactions employing an artificial intelligence workflow. *eLife*, 8, e40560.
- Gilmore, T. D. (2006). Introduction to NF- $\kappa$ B: Players, pathways, perspectives. *Oncogene*, 25, 6680–6684.

- Godinez, W. J., Hossain, I., Lazic, S. E., Davies, J. W., & Zhang, X. (2017). A multi-scale convolutional neural network for phenotyping high-content cellular images. *Bioinformatics*, 33, 2010–2019.
- Groen, F. C. A., Young, I. T., & Ligthart, G. (1985). A comparison of different focus functions for use in autofocus algorithms. *Cytometry*, 6, 81–91.
- He, K., Zhang, X., Ren, S., & Sun, J. (2016). Deep residual learning for image recognition. In *Proceedings of the IEEE Computer Society Conference on Computer Vision and Pattern Recognition* (pp. 770–778). Las Vegas, NV: IEEE Computer Society.
- Hung, J., Goodman, A., Ravel, D., Lopes, S. C. P., Rangel, G. W., Nery, O. A., ... Carpenter, A. E. (2020). Keras R-CNN: Library for cell detection in biological images using deep neural networks. *BMC Bioinformatics*, 21, 300.
- Kraus, O. Z., Ba, J. L., & Frey, B. J. (2016). Classifying and segmenting microscopy images with deep multiple instance learning. *Bioinformatics*, 32, i52–i59.
- Kraus, O. Z., Grys, B. T., Ba, J., Chong, Y., Frey, B. J., Boone, C., & Andrews, B. J. (2017). Automated analysis of high-content microscopy data with deep learning. *Molecular Systems Biology*, 13, 924.
- Krizhevsky, A., Sutskever, I., & Hinton, G. E. (2012). ImageNet classification with deep convolutional neural networks. In *Proceedings of the 25th International Conference Neural Information Processing Systems* (Vol. 1, pp. 1097–1105). New York, NY: Association for Computing Machinery.
- Kühbacher, A., Emmenlauer, M., Råmo, P., Kafai, N., Dehio, C., Cossart, P., & Pizarro-Cerdá, J. (2015). Genome-wide siRNA screen identifies complementary signaling pathways involved in listeria infection and reveals different Actin nucleation mechanisms during listeria cell invasion and Actin comet tail formation. *mBio*, 6, e00598–15.
- LeCun, Y., Bengio, Y., & Hinton, G. (2015). Deep learning. *Nature*, 521, 436–444.
- LeCun, Y., Bottou, L., Bengio, Y., & Haffner, P. (1998). Gradient-based learning applied to document recognition. *Proceedings of the IEEE*, 86, 2278–2324.
- Litjens, G., Kooi, T., Bejnordi, B. E., Setio, A. A. A., Ciampi, F., Ghafoorian, M., ... Sánchez, C. I. (2017). A survey on deep learning in medical image analysis. *Medical Image Analysis*, 42, 60–88.
- Matula, P., Kumar, A., Wörz, I., Erfle, H., Bartenschlager, R., Eils, R., & Rohr, K. (2009). Single-cell-based image analysis of high-throughput cell array screens for quantification of viral infection. *Cytometry Part A*, 75A, 309–318.
- May, R. C., Stone, N. R. H., Wiesner, D. L., Bicanic, T., & Nielsen, K. (2016). Cryptococcus: From environmental saprophyte to global pathogen. *Nature Reviews. Microbiology*, 14, 106–117.
- Meijering, E., Carpenter, A. E., Peng, H., Hamprecht, F. A., & Olivo-Marin, J. C. (2016). Imagining the future of bioimage analysis. *Nature Biotechnology*, 34, 1250–1255.
- Nichols, J. A., Herbert Chan, H. W., & Baker, M. A. B. (2019). Machine learning: Applications of artificial intelligence to imaging and diagnosis. *Biophysical Reviews*, 11, 111–118.
- Nielsen, M. (2015) *Neural networks and deep learning*. San Francisco, CA: Determination Press.
- Osaka, I., Hills, J. M., Kieweg, S. L., Shinogle, H. E., Moore, D. S., & Hefty, P. S. (2012). An automated image-based method for rapid analysis of Chlamydia infection as a tool for screening antichlamydial agents. *Antimicrobial Agents and Chemotherapy*, 56, 4184–4188.
- Ouyang, W., Aristov, A., Lelek, M., Hao, X., & Zimmer, C. (2018). Deep learning massively accelerates super-resolution localization microscopy. *Nature Biotechnology*, 36, 460–468.
- Pärnamaa, T., & Parts, L. (2017). Accurate classification of protein subcellular localization from high-throughput microscopy images using deep learning. *G3-Genes Genomes Genetics*, 7, 1385–1392.
- Pegoraro, G., & Misteli, T. (2017). High-throughput imaging for the discovery of cellular mechanisms of disease. *Trends in Genetics*, 33, 604–615.
- Pelt, D. M. (2020). Tackling the challenges of bioimage analysis. *eLife*, 9, e64384.
- Pernas, L., Adomako-Ankomah, Y., Shastri, A. J., Ewald, S. E., Treeck, M., Boyle, J. P., & Boothroyd, J. C. (2014). Toxoplasma effector MAF1 mediates recruitment of host mitochondria and impacts the host response. *PLoS Biology*, 12, e1001845.
- Pilla-Moffett, D., Barber, M. F., Taylor, G. A., & Coers, J. (2016). Interferon-inducible GTPases in host resistance, inflammation and disease. *Journal of Molecular Biology*, 428, 3495–3513.
- Ronneberger, O., Fischer, P., & Brox, T. (2015). U-net: Convolutional networks for biomedical image segmentation. In *Lecture notes in computer science (including subseries lecture notes in artificial intelligence and lecture notes in bioinformatics)* (pp. 234–241). Heidelberg, Germany: Springer Verlag.
- Rosowski, E. E., Lu, D., Julien, L., Rodda, L., Gaiser, R. A., Jensen, K. D. C., & Saeji, J. P. J. (2011). Strain-specific activation of the NF- $\kappa$ B pathway by GRA15, a novel *Toxoplasma gondii* dense granule protein. *The Journal of Experimental Medicine*, 208, 195–212.
- Roth, H. R., Shen, C., Oda, H., Oda, M., Hayashi, Y., Misawa, K., & Mori, K. (2018). Deep learning and its application to medical image segmentation. *Medical Imaging Technology*, 36, 63–71.
- Rudman, J., Evans, R. J., & Johnston, S. A. (2019). Are macrophages the heroes or villains during cryptococcosis? *Fungal Genetics and Biology*, 132, 103261.
- Russakovsky, O., Deng, J., Su, H., Krause, J., Satheesh, S., Ma, S., ... Fei-Fei, L. (2015). ImageNet large scale visual recognition challenge. *International Journal of Computer Vision*, 115, 211–252.
- Schindelin, J., Arganda-Carreras, I., Frise, E., Kaynig, V., Longair, M., Pietzsch, T., ... Cardona, A. (2012). Fiji: An open-source platform for biological-image analysis. *Nature Methods*, 9, 676–682.
- Schmidt, U., Weigert, M., Broaddus, C., & Myers, G. (2018). Cell detection with star-convex polygons. In *Lecture notes in computer science (including subseries lecture notes in artificial intelligence and lecture notes in bioinformatics)* (pp. 265–273). Heidelberg, Germany: Springer Verlag.
- Segebarth, D., Griebel, M., Stein, N., von Collenberg, C. R., Martin, C., Fiedler, D., ... Schoeffler, V. (2020). On the objectivity, reliability, and validity of deep learning enabled bioimage analyses. *eLife*, 9, e59780.
- Shorten, C., & Khoshgoftaar, T. M. (2019). A survey on Image Data Augmentation for Deep Learning. *Journal of Big Data*, 6, 60.
- Smith, K., Piccinini, F., Balassa, T., Koos, K., Danka, T., Azizpour, H., & Horvath, P. (2018). Phenotypic image analysis software tools for exploring and understanding big image data from cell-based assays. *Cell Systems*, 6, 636–653.
- Spiers, H., Songhurst, H., Nightingale, L., Folter, J. de, Hutchings, R., Peddie, C. J., ... Jones, M. L. (2020). Citizen science, cells and CNNs – Deep learning for automatic segmentation of the nuclear envelope in electron microscopy data, trained with volunteer segmentations. *bioRxiv*. Retrieved from <https://doi.org/10.1101/2020.07.28.223024>
- Srikanta, D., Santiago-Tirado, F. H., & Doering, T. L. (2014). *Cryptococcus neoformans*: Historical curiosity to modern pathogen. *Yeast*, 31, 47–60.
- Stöter, M., Niederlein, A., Barsacchi, R., Meyenhofer, F., Brandl, H., & Bickle, M. (2013). CellProfiler and KNIME: Open source tools for high content screening. In *Methods in molecular biology* (pp. 105–122). Totowa, NJ: Humana Press.
- Stringer, C., Wang, T., Michaelos, M., & Pachitariu, M. (2021). Cellpose: A generalist algorithm for cellular segmentation. *Nature Methods*, 18, 100–106.
- Sun, Y., Duthaler, S., & Nelson, B. J. (2004). Autofocusing in computer microscopy: Selecting the optimal focus algorithm. *Microscopy Research and Technique*, 65, 139–149.
- Tinevez, J. Y., Perry, N., Schindelin, J., Hoopes, G. M., Reynolds, G. D., Laplantine, E., ... Eliceiri, K. W. (2017). TrackMate: An open and extensible platform for single-particle tracking. *Methods*, 115, 80–90.
- Traver, M. K., Henry, S. C., Cantillana, V., Oliver, T., Hunn, J. P., Howard, J. C., ... Taylor, G. A. (2011). Immunity-related GTPase M (IRGM) proteins influence the localization of guanylate-binding protein 2 (GBP2) by modulating macroautophagy. *The Journal of Biological Chemistry*, 286, 30471–30480.

- Usaj, M. M., Styles, E. B., Verster, A. J., Friesen, H., Boone, C., & Andrews, B. J. (2016). High-content screening for quantitative cell biology. *Trends in Cell Biology*, *26*, 598–611.
- Voelz, K., Johnston, S. A., Rutherford, J. C., & May, R. C. (2010). Automated analysis of cryptococcal macrophage parasitism using GFP-tagged cryptococci. *PLoS One*, *5*, e15968.
- Weigert, M., Schmidt, U., Boothe, T., Müller, A., Dibrov, A., Jain, A., ... Myers, E. W. (2018). Content-aware image restoration: Pushing the limits of fluorescence microscopy. *Nature Methods*, *15*, 1090–1097.
- Yang, S. J., Berndl, M., Ando, D. M., Barch, M., Narayanaswamy, A., Christiansen, E., ... Nelson, P. (2018). Assessing microscope image focus quality with deep learning. *BMC Bioinformatics*, *19*, 77.

## SUPPORTING INFORMATION

Additional supporting information may be found online in the Supporting Information section at the end of this article.

**How to cite this article:** Fisch D, Evans R, Clough B, Byrne SK, Channell WM, Dockterman J, Frickel E-M. HRMAN 2.0: Next-generation artificial intelligence-driven analysis for broad host–pathogen interactions. *Cellular Microbiology*. 2021;23:e13349. <https://doi.org/10.1111/cmi.13349>